Divergent behavior of hydrothermal plumes in fresh versus salty icy ocean worlds

Suyash Bire[1], Tushar Mittal[2], Wanying Kang[3], Ali Ramadhan[1], Philip Tuckman[4], Christopher R German[5], Andreas M. Thurnherr[6], and John C Marshall[1]

[1]Massachusetts Institute of Technology
[2]Pennsylvania State University
[3]MIT
[4]Unknown
[5]Wood Hole Oceanographic Institution
[6]Lamont-Doherty Earth Observatory

January 17, 2023

Abstract

Water parcels close to their freezing point contract and become heavy on warming if they are sufficiently fresh, but expand and become buoyant when salty. We explore the resulting divergent behavior of hydrothermal plumes in fresh verses salty icy ocean worlds, with particular emphasis on Enceladus and Europa. Salty oceans develop buoyant plumes which rise upwards in the water column when energized by localised hydrothermal vents. Fresh oceans, instead, develop bottom-hugging gravity currents when heated near the freezing point, because of the anomalous contraction of fluid parcels on warming. The contrasting dynamics are highlighted and the implications discussed.

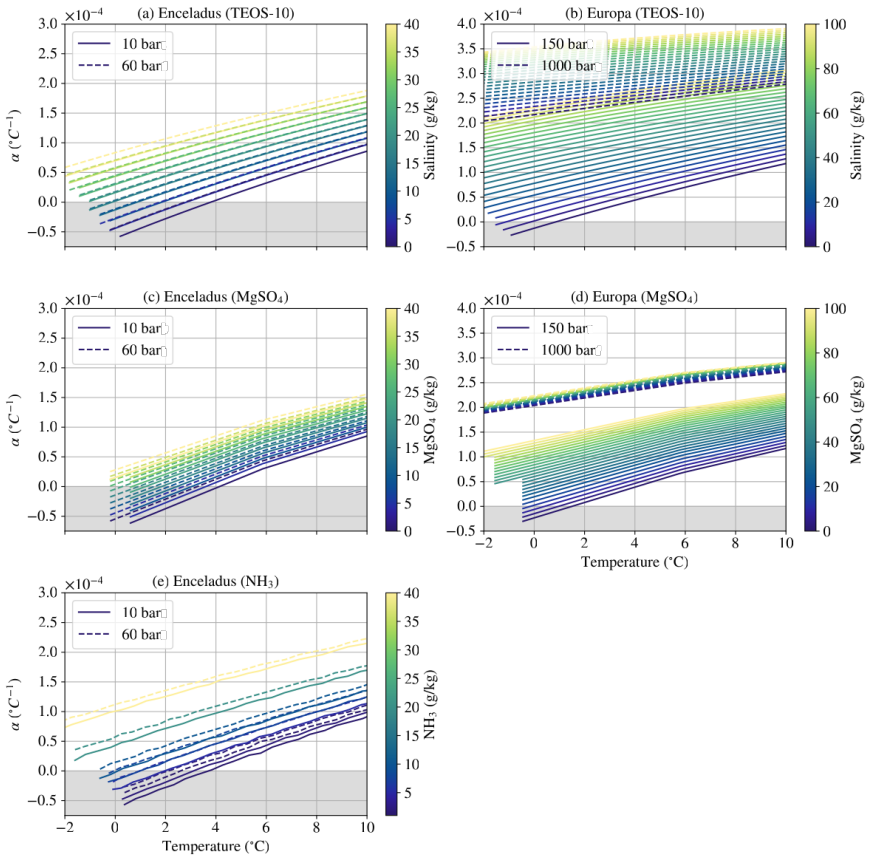

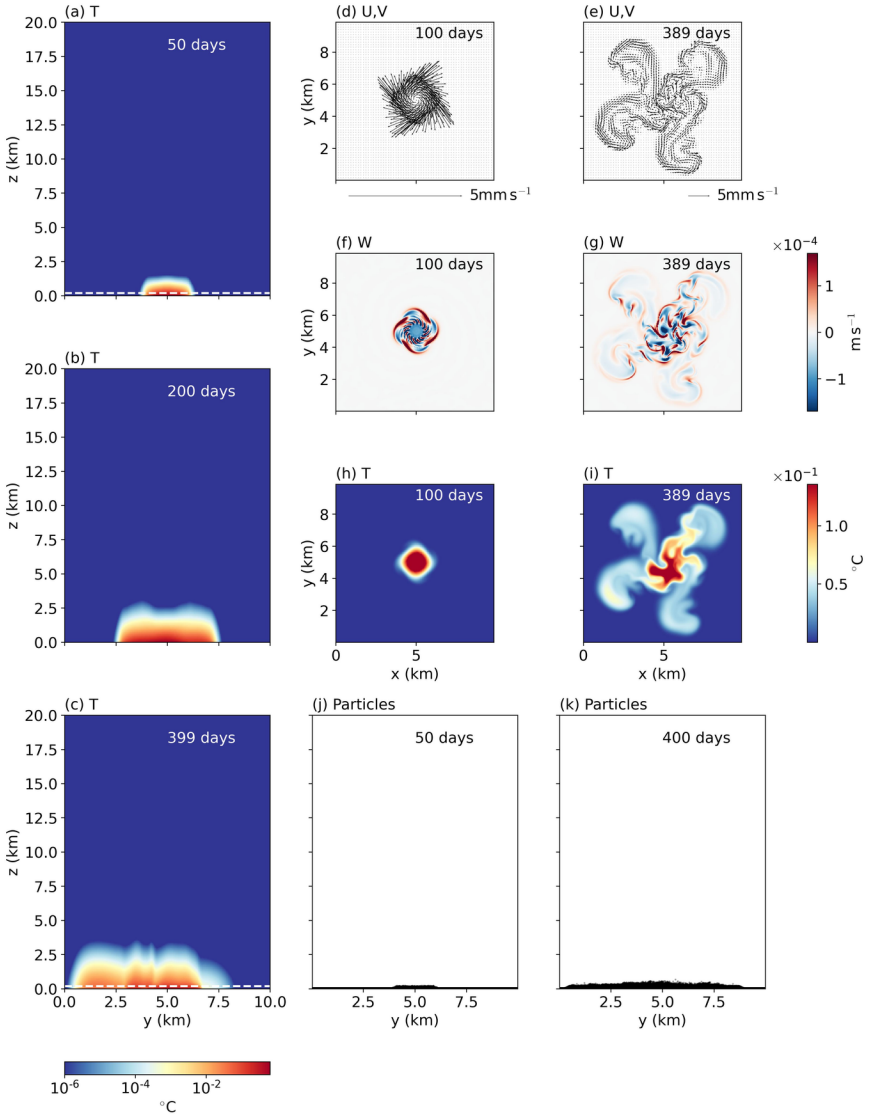

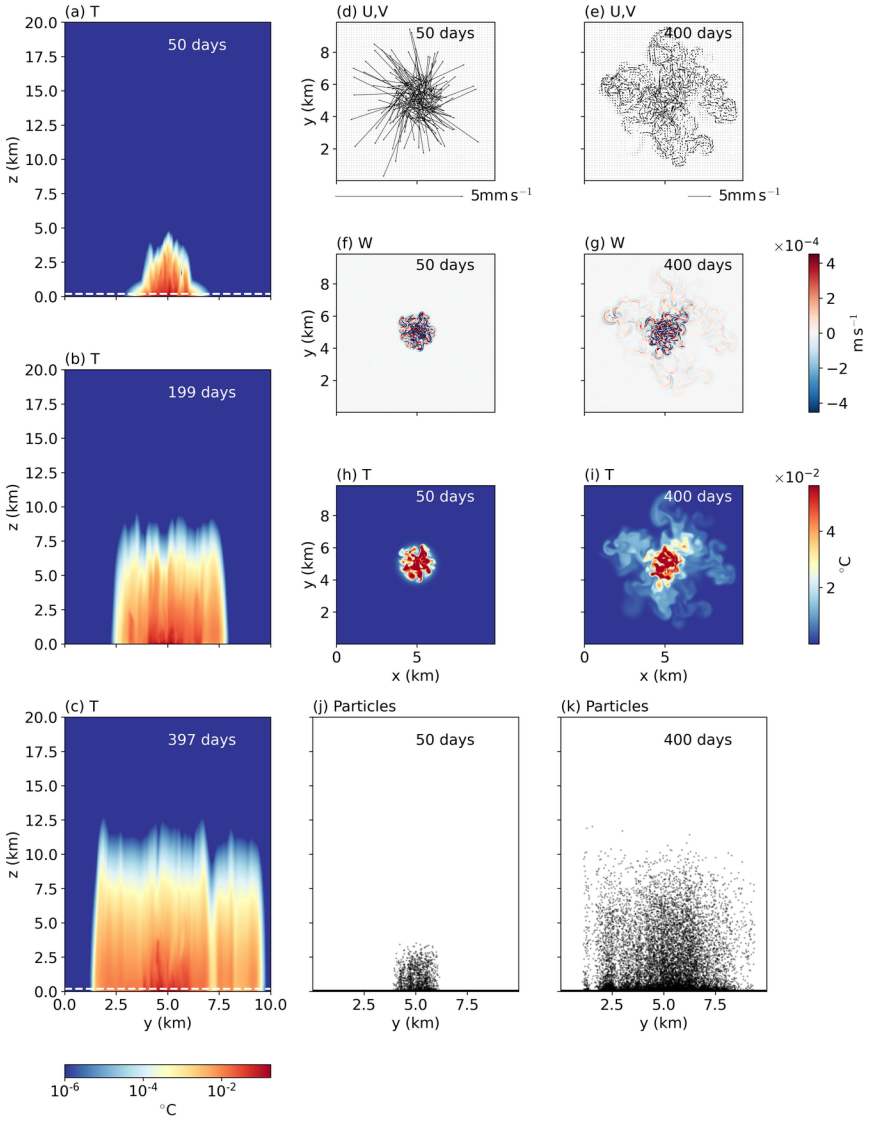

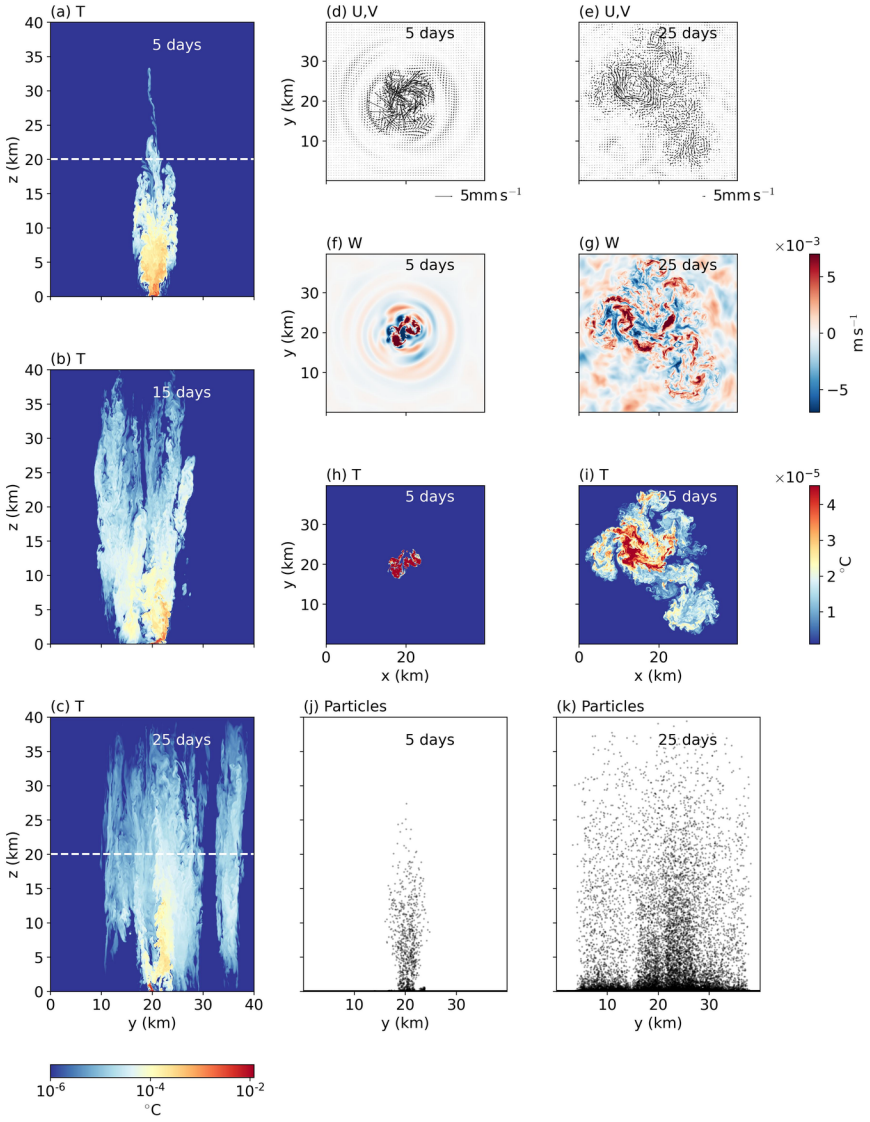

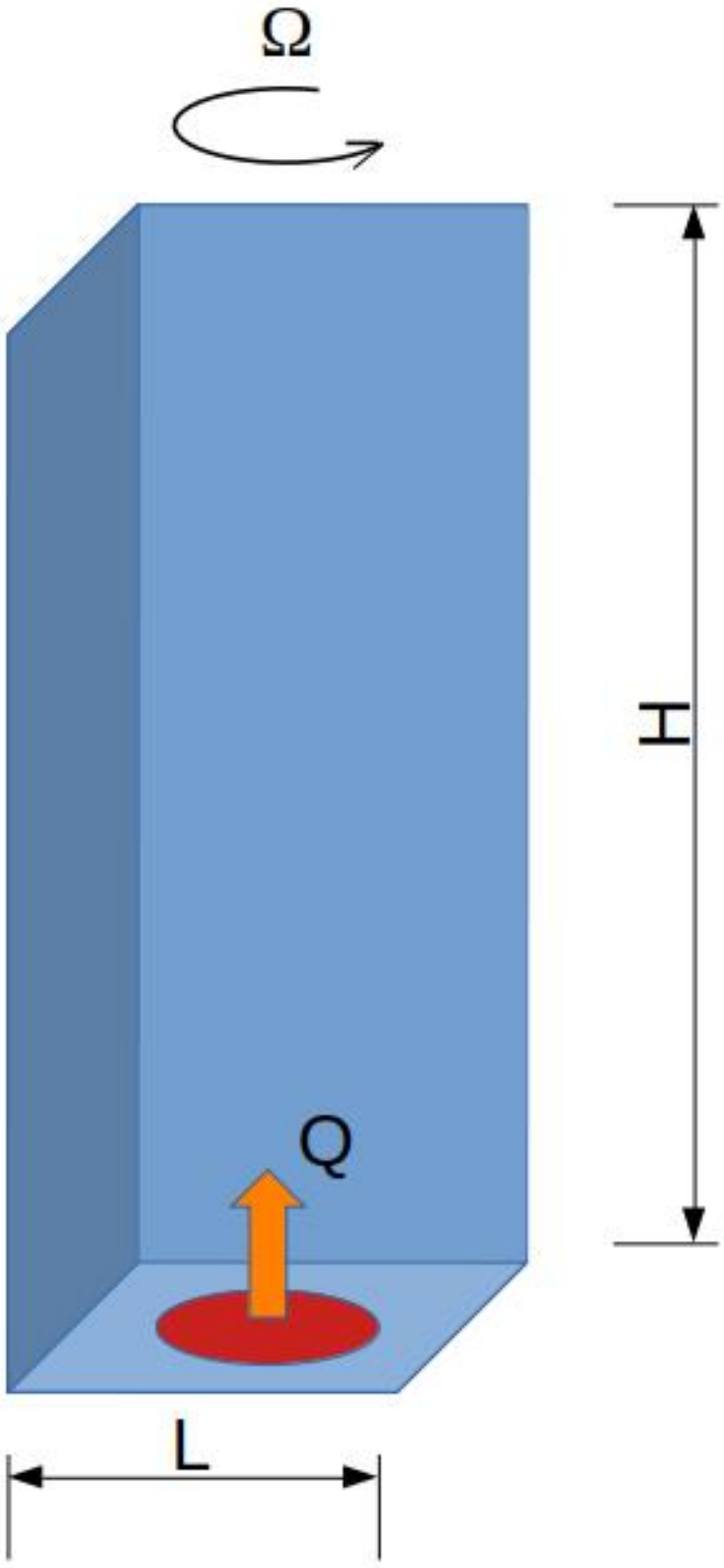

Divergent behavior of hydrothermal plumes in fresh versus salty icy ocean worlds

Suyash Bire[1], Tushal Mittal[1], Wanying Kang[1], Ali Ramadhan[1], Philip J. Tuckman[1], Christopher R. German[2], Andreas Thurnherr[3], John Marshall[1]

[1]Earth, Atmospheric, and Planetary Sciences, Massachusetts Institute of Technology, Cambridge, MA 02139 US
[2]Woods Hole Oceanographic Institution, 266 Woods Hole Road, Woods Hole, MA 02543-1050
[3]Lamont-Doherty Earth Observatory, 61 Route 9W , Palisades, NY 10964

Key Points:

- Salty oceans near the freezing point develop buoyant plumes which rise in the water column when energised by localised hydrothermal vents.
- Buoyant plumes become diluted by turbulence and baroclinic instability as they rise upwards.
- Fresh oceans develop bottom-hugging currents when heated near the freezing point, because of the contraction of fluid parcels on warming.

Corresponding author: Suyash Bire, `bire@mit.edu`

Abstract

Water parcels close to their freezing point contract and become heavy on warming if they are sufficiently fresh, but expand and become buoyant when salty. We explore the resulting divergent behavior of hydrothermal plumes in fresh verses salty icy ocean worlds, with particular emphasis on Enceladus and Europa. Salty oceans develop buoyant plumes which rise upwards in the water column when energized by localised hydrothermal vents. Fresh oceans, instead, develop bottom-hugging gravity currents when heated near the freezing point, because of the anomalous contraction of fluid parcels on warming. The contrasting dynamics are highlighted and the implications discussed.

Plain Language Summary

Oceans on icy moons such as Enceladus and Europa may potentially have many of the conditions required for life. The possible existence of hydrothermal vents on the ocean floors of these moons are prime candidates as sources of biological activity. Here we explore the conditions in which heating at bottom vents might lead to convection that could carry biomarkers from the bottom of the ocean up to the ice. We argue that if the background salinity is low, heating close to the freezing point of water leads to dense, bottom-hugging density currents. If the water is salty, however, upward-reaching plumy convection can result.

1 Introduction

Since the Cassini mission, Enceladus has become a prominent astrobiological target with potentially many of the conditions required for habitability (Cable et al., 2021; Glass et al., 2022; Hand et al., 2020). Enceladus is an archetype of a broader class of icy ocean worlds, a number of which may also be habitable (Nimmo & Pappalardo, 2016; Vance et al., 2018). Early observations of geological features on its ice shell led to speculations on the presence of an active subsurface ocean (Nimmo & Pappalardo, 2016). The subsequent discovery of plumes emanating from the south pole of Enceladus boosted the idea that Enceladus might posses a significant subsurface ocean (Porco et al., 2006; Hansen et al., 2006). Observations and modeling studies of exaggerated libration on Enceladus, along with gravity-topography analysis, have all but confirmed the presence of a global subsurface ocean with an average thickness of 35 - 45 km (e.g. Thomas et al., 2016; Čadek et al., 2016; Van Hoolst et al., 2016; Beuthe et al., 2016; Hemingway & Mittal, 2019). Additionally, studies of the composition of the plumes have indicated the presence of silica nanoparticles (Hsu et al., 2015; Sekine et al., 2015), hydrogen (Waite et al., 2017), as well as salts and organic compounds (Postberg et al., 2018; Fifer et al., 2022). The actual salinity of the ocean is still a matter of debate.

Such observations are suggestive of active hydrothermal activity, with Enceladus's rocky core providing the thermochemical energy for potential life at/beneath the seafloor (Choblet et al., 2021). Furthermore, Choblet et al. (2017) show that if the porous rocky core (20-30 % porosity e.g. Hemingway and Mittal (2019)) is highly dissipative, core-scale porous media convection might focus hydrothermal activity at the poles. Rovira-Navarro et al. (2022) find qualitatively similar results for Enceladus's core using a poro-viscoelastic rheology. However, viscous dissipation in the core can drive geological activity only if it has a low rigidity and viscosity. Choblet et al. (2017) also suggest, using scaling results from Goodman and Lenferink (2012), that hydrothermal heat localization could be sufficient to power hydrothermal plumes all the way up to the ice-ocean interface on a timescale of months.

In contrast to the aforementioned observational/porous flow modeling for Enceladus, most studies of convection or hydrothermal plume dynamics on icy moons have focused on Europa and/or have prescribed high seafloor heat fluxes (Goodman et al., 2004;

Goodman & Lenferink, 2012; Soderlund et al., 2013; Ashkenazy & Tziperman, 2021; Bire et al., 2022). For example, Goodman et al. (2004) conducted laboratory experiments and derived scaling laws to predict the timescale over which plumes from the bottom of Europa's ocean would reach the surface. Additionally, they show that any given plume's life cycle would involve an initial transient stage when the effects of planetary rotation are not felt, an intermediate stage where the plume rises to the surface in a cylindrical column, and a final stage in which the plume becomes baroclinically unstable and sheds secondary vortices. The main outcome was that predictions could be made about the efficiency of heat transfer from the sea floor to the base of the ice shell. Goodman and Lenferink (2012) tested these findings through numerical simulations. One such simulation is repeated here. Both of these studies suggest that plumes might transport about 0.1 to $10\,\mathrm{W\,m^{-2}}$ from the seafloor to the base of the ice shell and span diameters of $O(10\,\mathrm{km})$. Note that these models used heat fluxes which are significantly larger than that which is nominally expected on Europa and Enceladus (Choblet et al., 2017).

Based on these findings, as well as models of hydrothermal circulation in icy ocean worlds (e.g., Choblet et al. (2017) and Steel et al. (2017) for Enceladus, Běhounková et al. (2021) for Europa) it has been assumed that for an unstratified/weakly stratified ocean, hydrothermal plumes might traverse the ocean almost vertically on timescales of days-months. This paradigm provided the framework for the interpretation of geochemical measurements of plume particles on Enceladus and for the spectroscopy of surface material on Europa/other icy ocean worlds. For example, Hsu et al. (2015) observe silica nanoparticles in plume ejecta from the south pole of Enceladus. Hsu et al. (2015) and Sekine et al. (2015) posited that these particles originated from hydrothermal reactions in the rocky core and transited across the Enceladean ocean of thickness of $O(10\,\mathrm{km})$ in a matter of days-weeks. In order to match observational constraints on particle size, these studies also constrain the salinity of the Enceladean ocean, suggesting it to be less than 4%(or $40\,\mathrm{g\,kg^{-1}}$ or 40 psu). In addition, this paradigm of fast hydrothermal plume transport is also the basis of models explaining various surface geological features or surface shell thickness variations on icy satellites (e.g. Čadek et al., 2019; Kvorka et al., 2018) using model results from solid core processes. Finally, an efficient transport from seafloor to ice shell (and potentially to the surface through jets or other cryovolcanism) is a key motivator for future space missions to these bodies seeking extraterrestrial life, especially mission concepts arguing for landing on the ice shell and scooping surface material deposited by the plumes (Choblet et al., 2021; MacKenzie et al., 2022). Typically, it has been assumed that, in analogy with deep sea hydrothermal vents on Earth, the seafloor on icy ocean worlds is likely the most habitable environment on such bodies.

To the best of our understanding, previous studies have yet to focus on one key geophysical characteristic of hydrothermal plume dynamics: the influence of ocean salinity and the equation of state (EOS) of water near the freezing point of water. Previous work has analyzed the role of salinity on the large scale circulation of icy ocean worlds and shown it to be a key parameter affecting the circulation (Kang et al., 2022; Zeng & Jansen, 2021). As argued by Kang et al. (2022), the most likely salinity for icy ocean worlds with shell thickness variation typical of Enceladus is of intermediate value (that is less than 20 psu (g/kg), see later summary). However, most previous work assumes larger ocean salinities, more typical of Earth's ocean. In this case seawater heated near its freezing point becomes lighter than the surroundings and hence rises. In contrast, at lower salinities, heating of water close to freezing temperatures, actually makes water denser, due to the anomalous expansion of near-freezing water (Ede, 1956; Ivanov & Nikolov, 2020). In this case, convective plumes driven by core hydrothermal activity are unlikely to directly reach the surface.

The purpose of this study is to directly address the role of salinity in shaping the response of the ocean to hydrothermal heat sources in a parameter space of relevance to icy moons. In section 2, we explore the EOS and the effect of salinity and pressure

on the thermal expansion coefficient of seawater. Sections 4 and 5 contrast the behavior of hydrothermal plumes in the cases where the thermal expansion coefficient is positive and negative, respectively. Section 6 discusses the implications of our study for various icy moons. The numerical simulations designed to study hydrothermal plume dynamics in a nominally Enceladus-like icy moon are described in the supporting information.

2 Thermal expansion coefficient of water

One of the key variables that determines the dynamics of hydrothermal plumes is the thermal expansion coefficient of water since this controls the buoyancy of fluid parcels upon heating. The thermal expansion coefficient of water depends on, amongst other things, the amount and type of dissolved solute. Early estimates of the salinity of Enceladus' ocean are based on assumptions of thermodynamic equilibrium. Considering a range of hydrothermal and freezing conditions for chondritic compositions, an ocean in equilibrium with the rocky core will have a present day salinity of between 2-20 psu (Zolotov, 2007; Zolotov & Postberg, 2014; Glein et al., 2018a). However, at least ~ 17 psu may be required to keep the geysers' liquid–gas interface convectively active ensuring that they do not freeze up (Ingersoll & Nakajima, 2016). Sodium-enriched samples taken by Cassini from south pole sprays have a salinity of 5-20 psu. This can be considered a lower bound since the interaction of cold water vapor sprays with their environment may lower the salinity of droplets through condensation (Postberg et al., 2009). There is considerable uncertainty, however, since fractional crystallization and disequilibrium chemistry may partition components in such a way that geyser particles are not directly representative of the underlying ocean (Fox-Powell & Cousins, 2021). Furthermore, if particles originate from a hydrothermal vent, composition can deviate far from that of the overall ocean (Glein et al., 2018a; Fifer et al., 2022). It is of note that the size of silica nano-particles carried along in the sprays has also been used to estimate ocean salinity. Assuming an intermediate value of pH and a short transport timescale induced by hydrothermal activity, a salinity < 40 psu is obtained (Hsu et al., 2015). In a separate line of argument, oceans with too much or too little salt may have a strong ice pump effect, leading to the erosion of ice thickness gradients (Kang et al., 2022). Europa's ocean salinity is even more poorly constrained. The amplitude of the magnetic induction signal suggests a rather salty (¿ 50 psu), deep ocean. However, significant degeneracy exists in the retrieval process (Hand & Chyba, 2007) and there is uncertainty about the effect of accreted volatiles (CO_2, NH_3) on ocean conductivity.

The specific chemical composition of the plumes erupting from the south pole of Enceladus' ice shell is also an ongoing field of study (Glein et al., 2018b; Khawaja et al., 2019; Fifer et al., 2022; Postberg et al., 2022). Sodium chloride inferred from plume measurements yields information about the salinity of the ocean on Enceladus (Postberg et al., 2009; Glein et al., 2018b). Spectroscopy of the plumes has also indicated the presence of ammonia Waite et al. (2017), along with other volatile species. The composition of Europa's ocean is similarly uncertain. Trumbo et al. (2019) report evidence for sodium chloride on Europa's ice crust. Moreover, modeling studies of composition of Europa's ocean suggest that it might be enriched in metallic salts such as magnesium sulphate (Vance et al., 2018). Given the distinct initial sate and evolutionary history of icy moons, the composition of seawater therein could be very distinct from that on earth: the terrestrial EOS may not be relevant. Given these possibilities, we now briefly explore the range of likely thermal expansion coefficients of water under varying temperatures, pressures, and compositions.

We first contrast the thermal expansion coefficient of the ocean on Enceladus (fig. 1a) with that of Europa (fig. 1b), assuming that an EOS for NaCl dominated water such as that on Earth's ocean (TEOS-10) is appropriate (Millero et al., 2008; Roquet et al., 2015). Similarly, in panels c and d we also plot the likely variation of the thermal expansion co-

efficient on Enceladus and Europa assuming a magnesium sulphate solute using the *PlanetProfile* algorithm (Vance et al., 2014). Panel e shows the effect of ammonia on thermal expansion coefficient on Enceladus.

The first pattern to note in all panels is that the thermal expansion coefficient at any given temperature and pressure increases with the concentration of salt. The presence of ionic compounds in water disrupts its tendency to form hydrogen bonds and causes it to expand on heating. Thus, at high concentrations of salts, the thermal expansion coefficient of ocean water is always positive. However, at low salt concentrations, we do see negative values of α between temperatures of -2 to 4°C in panels a, c, and e. Thus, fresher oceans result in anomalous behavior in which water close to freezing becomes denser upon heating.

A second pattern can be seen in fig. 1: panels b and d show that negative values of thermal expansion coefficient are only attained at low values of pressure on Europa. This behavior results from non-linearities in the equation of state and especially their sensitivity to pressure. Since Europa's gravity is about 10 times stronger than that of Enceladus, pressure increases more rapidly with depth on Europa. Assuming ice shell thickness on Enceladus and Europa to be 30 km and 10 km, respectively, the hydrostatic pressure at a depth of 5 km from the base of the ice shell on Enceladus is 10 bar while that on Europa is 150 bar. This difference becomes larger the deeper we go. Therefore, in panels b and d, we see that the high pressures at deeper levels in Europa's ocean suppress anomalous contraction of water under warming.

A key conclusion of our EOS survey is that for high salinity Europa-like oceans, the effect of salinity is not likely to suppress buoyant, plumy dynamics triggered by bottom heating. This is true regardless of whether the ocean is dominated by chloride or sulfate salts or high ammonia concentrations. On the other hand, in the case of Enceladus, typical values of salinity estimated from previous studies (Hsu et al., 2015; Kang et al., 2022) can place it in the region of negative alpha. While large concentrations of ammonia lead to a positive thermal expansion coefficient, small amounts can lead to a negative limit for alpha. This is especially important for Enceladus because best current estimates of ammonia concentrations there are $4 - 13\ \mathrm{g\,kg^{-1}}$ (assuming seawater composition is the direct volume mixing gas abundance ratios in the plume) (Waite et al., 2017) and $0.1 - 2\ \mathrm{g\,kg^{-1}}$ when accounting for fractionation of gas plume composition due to water vapor condensation and gas exsolution (Fifer et al., 2022). At such concentrations, especially when accounting for gas fractionation, Enceladus's ocean could indeed be in the negative alpha regime.

3 Numerical explorations of hydrothermal plumes on fresh versus salty icy ocean worlds

We explore by numerical experimentation how the anomalous contraction of water warmed near its freezing point impacts the dynamics of hydrothermal plumes. We use *Oceananigans.jl*, a state-of-the-art ocean general circulation model written in Julia to run fast on graphical processing units (Ramadhan et al., 2020), configured for study of hydrothermal plumes run at high-resolution. The domain stretches from 0 to L in both zonal (x) and meridional (y) directions and from $z = -H$ to $z = 0$ in the vertical direction as shown in fig. 2. L and H are set to 10 km and 40 km, respectively, in our two experiments for Enceladus-like parameters. The grid is rectilinear with a spacing of 40 m in the horizontal and 80 m in the vertical direction. For our experiment with Europa-like parameters, L is extended to 40 km and the horizontal grid spacing is set to 80 m. These values for the domain size, and consequently the grid spacing, are chosen based on the horizontal scale of the plumes. The periodic nature of the domain means that if the domain is too small the plumes self-interact even before they are fully developed. The

results in this study are not sensitive to the choice of these parameters as long as the horizontal domain size is wide enough to represent a fully evolved plume.

The rotation rate is $\Omega = 5.3\times10^{-5}\,\mathrm{s}^{-1}$, acceleration due to gravity is $g = 0.1\,\mathrm{m\,s}^{-2}$, and specific heat capacity is $C_\mathrm{P} = 4000\,\mathrm{J\,kg}^{-1}\,\mathrm{K}^{-1}$: all values are suitable for Enceladus (Soderlund, 2019). The horizontal and vertical Laplacian diffusivity is $1.25\times10^{-3}\,\mathrm{m}^2\,\mathrm{s}^{-1}$ and $5\times10^{-3}\,\mathrm{m}^2\,\mathrm{s}^{-1}$, respectively. The values are chosen such that they ensure numerical stability as well as preserve baroclinic turbulence important for our study. The Prandtl number is 1.

To illustrate the importance of different salinities, we perform two simulations with salinities of 15 psu and 35 psu which imply a different sign of thermal expansion coefficient. At the bottom, $z = -H$, a patch of heating is prescribed thus:

$$Q = Q_0\,\exp\left[-\frac{(x-x_0)^2+(y-y_0)^2}{2\,\sigma^2}\right], \tag{1}$$

where $x_0 = y_0 = L/2$ is at the center of the domain and $\sigma = l/\sqrt{2\pi}$ controls the width of the heating patch. For our simulations we set l to 1000 m and Q_0 to $100\,\mathrm{W\,m}^{-2}$. The choice of l and Q_0 is informed by the predicted seafloor heat flux and its localization. The choice of these parameters does not affect the overall conclusions of this study. With the values we have chosen the total heat flux entering the domain is

$$E = \int\int Q\,\mathrm{d}x\,\mathrm{d}y = Q_0\,l^2, \tag{2}$$

which is $10^8\,W = 0.1\,GW$. If averaged over the entire cross section we obtain $1\,\mathrm{W\,m}^{-2}$. This value is $\sim$ 10-20 times that suggested by Choblet et al. (2017) which means that we are applying more heat localization than suggested by them. Applying a lower heat flux in line with what they suggested does not change the findings of this study. The heat flux is applied as a temperature flux.

We employ the 55 term polynomial approximation to the TEOS-10 proposed by Roquet et al. (2015). The pressure used in the expressions is scaled by the ratio of Enceladus's gravity to that of the Earth. In the case of a linear equation of state, we can write the buoyancy flux as,

$$B = \alpha g \frac{Q}{\rho_0 C_\mathrm{P}}. \tag{3}$$

Note that the buoyancy flux changes sign based on the sign of α, that is, positive α produces buoyant water that tends to rise, while a negative α produces dense water that spreads along the bottom.

4 Buoyant plumes in saline oceans

Fig. 3 shows typical characteristics of a plume originating from a bottom-heated patch in a salty ocean in which $S = 35$ psu. The temperature and particles released in to the flow, as shown in panels b, c, j, and k, indicate that the influence of the bottom heating patch is to create plumes which rise to a height of roughly 10 km from the seafloor after 400 rotation periods or so. Based on previos studies one could imagine that water just above the heating patch would become more buoyant, even after entraining ambient water, and rise upward toward the surface. However, the plan views of horizontal and vertical currents and temperatures shown in panels d to i, reveal that swirling currents and eddies are created which also sweep warm fluid laterally, not just vertically, away from the heating source. It is for this reason that our plumes do not reach all the way up to the surface even after integrating for hundreds of rotation periods.

Under the influence of rotation, some of the vertical plume velocity attained by a buoyant water parcel is converted into horizontal motion thus inhibiting convection through

Table 1. Expected parameters for icy moons (Soderlund, 2019) and those used in our simulations are shown in this table. Acceleration due to gravity is g, thermal expansion coefficient is α, rotation rate of the moon is Ω, depth of the ocean is H, and heat flux emanating from the patch area is Q_0. The total heat entering the domain, E, is calulated using equation (2), the buoyancy flux, F, is calculated using (5), the rotational length scale, $l_{\rm rot}$, and Rossby number, Ro^*, are calculated using equations (6) and (4), respectively. *Note that heat flux at the bottom of Europa is not well constrained. We use a value of $10\,\mathrm{W\,m^{-2}}$ but it could range from 1 to $100\,\mathrm{W\,m^{-2}}$ (Běhounková et al., 2021).

		g $\mathrm{m\,s^{-2}}$	α $(10^{-4}\,\mathrm{K^{-1}})$	Ω $(10^{-5}\,\mathrm{s^{-1}})$	L (km)	H (km)	Q_0 $(\mathrm{W\,m^{-2}})$	E (GW)	F $(10^{-5}\,\mathrm{m^4\,s^{-3}})$	l_{rot} (m)	Ro^* (10^{-3})	Salinity (psu)
Icy moons	Europa	1.3	2.5	2.1		100	10*	0.01	79.93	322	3.22	50
	Enceladus	0.1	0.1	5.3		50	5	0.005	0.12	32	0.63	15
Simulations	Europa	1.3	3.0	1.0	40	40	100	0.1	959	1046	26.16	35
	Saline Enceladus	0.1	0.1	5.3	10	40	100	0.1	2.45	67	1.68	35
	Fresh Enceladus	0.1	0.1	5.3	10	40	100	0.1	2.45	67	1.68	15

lateral dilution. Following Speer and Marshall (1995) and Helfrich (1994), the influence of rotation on the buoyant plume can be expressed in terms of an appropriately defined natural Rossby number:

$$Ro^* = \frac{1}{H}\left(\frac{F}{f^3}\right)^{1/4}, \tag{4}$$

where

$$F = \int\int B \,\mathrm{d}x\,\mathrm{d}y \tag{5}$$

is the magnitude of the buoyancy flux integrated over the area of the heating patch with units of $(m^4 s^{-3})$, $f = 2\Omega$ is the rotation rate of the system, and H is the depth of the fluid — see (Jones & Marshall, 1993; Maxworthy & Narimousa, 1994; Goodman & Lenferink, 2012). The length scale

$$l_{\mathrm{rot}} = \left(\frac{F}{f^3}\right)^{1/4} \tag{6}$$

is a measure of the distance a buoyant parcel of fluid travels in a rotation period. Thus, the natural Rossby number can essentially be thought of as a ratio of two length scales, l_{rot} and H; if the ratio is small the depth of the ocean is much larger than the distance traveled by a heated parcel in one day, while if the ratio is large the parcel reaches the surface at height H before rotation can influence its motion. As discussed in Bire et al (2022), Ro^* has great utility because it only depends on externally-prescribed parameters which are somewhat constrained by observations and is independent of uncertain eddy viscosities and diffusivities which are set by the nature of unresolved and unobservable small-scale turbulence.

Table 1 sets out the values of key dimensional and non-dimensional parameters for hydrothermal activity on Enceladus and Europa, together with those same parameters for the numerical experiments presented here. Note that Enceladus, due to its small gravity and tiny thermal expansion coefficient, typically has very weak buoyancy forcing, F, (even after prescribing an order-of-magnitude more localization than suggested by Choblet et al. (2017)) and a very small value of Ro^*, roughly commensurate with the Ro^* pertaining to the experiment shown in Fig. 3. This should be contrasted with Europa which, due its larger gravity and larger expansion coefficient, has an F which is almost three orders of magnitude larger. Europa is also thought to be a considerably deeper ocean than Enceladus. These two factors lead to an Ro^* on Europa which is 5 times larger than that on Enceladus, although it remains much smaller than unity.

In the studies of Goodman and Lenferink (2012), a highly concentrated heat, and thus buoyancy flux, for Europa led to plumes reaching all the way up to the surface within $15 - 20$ days even after inhibition by rotation. For the purpose of cross comparison, we reproduce one of their calculations in Fig.4 which illustrates the response to larger buoyancy fluxes appropriate to Europa. Note that for the parameters assumed in Fig.4 (which are from one of the experiments in Goodman and Lenferink (2012)), representative of a high heat flux end-member for Europa, F is more than 100 times larger than is perhaps reasonable, and Ro^* order 10 times larger. In this case a plume rising from (and particles released from) a hydrothermal vent at the bottom travels all the way to the surface in several 10s of days. It is perhaps not implausible that some of the icy surface geomorphology seen on Europa could be evidence of hydrothermal activity from below.

But what happens if we assume that the water making up our ocean is very fresh rather than salty, with a negative expansion coefficient?

5 Bottom spreading gravity currents in fresh oceans

Fig. 5 shows typical flow patterns of plumes heated in a fresh ocean in which the salinity is set to 15 psu, near freezing temperatures. For icy moons like Enceladus, the

water is expected to be close to freezing temperatures which means that the coefficient of thermal expansion becomes negative. Thus, the water directly above the heating patch initially becomes warm and dense. Continuous heating from the warm patch provides an uninterrupted supply of dense water. As a result, the dense water initially spreads radially outwards along the bottom. A short while later, it comes under the influence of rotation and forms an anticyclonic circulation around the source (heating patch) as can be seen in Fig. 5d. Eventually, as more and more dense water is supplied from the patch, the outflow forms four secondary vortices (panels e, g, i). The temperature signature and the particles released at the bottom shown in panels c and k, respectively, further show that the plume does not become buoyant at least in the first 400 rotation periods.

Literature on continuously forced gravity currents is sparse but there is some literature on lock release experiments which is relevant to the present study (e.g. Saunders, 1973; Griffiths & Linden, 1981; Dai & Wu, 2016, 2018). Typically, they involve releasing a fluid of high or low density into another fluid of a background density in a rotating system. If a dense fluid is released into a fluid of low background density, it naturally settles at the bottom, while if the released fluid is light, it rises to the top. In the former case, the dense fluid has some effects due to bottom friction but the two cases are rather similar to one-another (Saunders, 1973). Such experiments allow us to study how these fluids of distinct densities transition to a stable state.

The difference in density provides a parameter known as the reduced gravity or buoyancy given by

$$g' = g\frac{\rho_1 - \rho_0}{\rho_0} = -b, \tag{7}$$

where g is the acceleration due to gravity and ρ_0 is the density of the background fluid and ρ_1 is that of the released fluid. Another crucial parameter is the volume of dense fluid released which is measured in terms of the radius of the cylinder, R, and its height, h. Most studies tend to use a cylindrical lock extending across the water column, H, which allows them to characterize the volume of fluid released in terms of R only. The Rossby radius of deformation,

$$l_\rho = \frac{\sqrt{g'H}}{f}, \tag{8}$$

gives a limiting length scale at which the propagating gravity waves are influenced by rotation. In the lock release experiments, the ratio of this length scale to that of the radius of the cylindrical lock, R, is proportional to the ratio of inertial to Coriolis terms in the momentum equation,

$$B = \frac{l_\rho^2}{R^2}. \tag{9}$$

where B is a Burger number. Depending on the value of B, the heavy fluid flowing outwards undergoes different dynamics. For low values of B, the Coriolis forces become important and the outflow breaks up into independent vortices, the vortex splitting described by Saunders (1973). For intermediate values, vortex wandering occurs in which the flow around the lock forms a vortex but it never detaches from the primary vortex and instead rotates around it. For high values of B, the Coriolis forces are small and the outflow reaches a maximum radius as the radial flow is diverted in the azimuthal direction and forms a bulbs-and-wedges pattern at the outer boundary (Dai & Wu, 2016, 2018).

Griffiths and Linden (1981) performed laboratory experiments in which they compared constant volume lock-release cases with constant flux cases (fluid is released at the top at a constant rate). In the constant flow rate case, they find that the light fluid spreads at the surface initially for $\sim 1-2$ rotation periods after which baroclinic instability develops on the near vertical interface between the light and dense fluid for the case of low B. The baroclinic instability is initially small but grows with time and imparts a non-axisymmetric nature to the flow. The non-axisymmetric component of the flow eventually grows to shed independent vortices from the main initial vortex. The number of new

vortices shed again depends on the ratio of Coriolis to buoyancy forces, as well as on the depth occupied by the injected flow. This behavior is qualitatively similar to results from our experiment in which the Rossby radius of deformation is order 100s of m and much smaller than the domain size (R), leading to a small value of B and hence vortex splitting.

Although Griffiths and Linden (1981) were able to characterize an empirical relationship between the number of secondary vortices and non-dimensional parameters such as B and h/H, their domain was horizontally constrained and boundary effects became significant. In addition, in their experiments, the depth of the injected flow may become comparable to the Ekman layer leading to substantial viscous effects. Both Saunders (1973) and Griffiths and Linden (1981) find that viscous effects facilitate secondary vortex formation in surface as well as bottom Ekman layers. Thus, further research needs to be undertaken to understand (i) the nature of vortex splitting in the constant flux case and (ii) the effect of Ekman layers and bottom friction on flow instability. Nevertheless, our results, when combined with existing work on forced gravity currents, suggests that hydrothermal plumes in a fresh ocean are likely to lead to the formation of unstable vortices of dense fluid near the seafloor. This scenario is very different from the plumy convection observed on heating a fluid in which the thermal expansion coefficient is positive. The choice of 15 psu here is based on TEOS-10 and has been chosen for illustrative purposes. In the real Enceladean ocean, as long as the salt composition and concentration allows anomalous contraction of water on heating, the bottom spreading case is likely to occur.

6 Discussion — Implications for icy moons

Our results highlight the critical role of seawater salinity and ocean depth on controlling hydrothermal plume dynamics in icy ocean worlds. In particular, we conclude that on Europa vents may induce "buoyant" hydrothermal plumes because the ocean is perhaps salty and deep, and so the thermal expansion coefficient positive: hydrothermal activity reminiscent of that on Earth will likely ensue, as studied for example in Goodman and Lenferink (2012). Enceladus, instead, may have "dense" hydrothermal activity due to it being fresher and shallower and thus possessing, perhaps, a negative thermal expansion coefficient: heavy fluid would then flow out from venting systems hugging the bottom. Owing to the resulting stable stratification and a steady supply of minerals from the core, the bottom dense layer could become chemically enriched. This mineral-rich dense layer and its interface with the lighter layer above, could potentially provide rich habitats for chemosynthetic life away from any liquid-solid interface like the base of the ice shell or the seafloor. It has long been known that chemosynthetic microbial activity can occur at chemical gradients in mid-water away from any liquid-solid interface, as described at redox interfaces in anoxic basins such as the Black Sea and Saanich Inlet since the 1980s (Tebo et al., 1984). The same processes are now recognized to also be present across large swathes of Earth's deep ocean basins within oxygen minimum zones, for example across much of the Eastern Tropical Pacific Ocean and across the Arabian Sea in northern Indian Ocean where a diversity of microbial metabolic niches are sustained. Since the Enceladus' rocky core likely has high porosity (Choblet et al., 2017), the dense hydrothermal fluid could also strongly affect the shallow porous flow in the core by enhancing fluid flow into the core. This could provide an additional mechanism to stimulate chemically-fuelled microbial activity in a deep sub-seafloor biosphere on Enceladus —- an area of research that is of particular current interest here on Earth (Cario et al., 2019).

It should be noted that our study has made a number of key simplifications. Our simulations were initialized from a state of rest and the background temperature of the entire water column is assumed to be at the freezing temperature of water just under the ice sheet. If we consider large scale ocean dynamics as well as long term dynamics

of hydrothermal plumes, the ambient water into which the hydrothermal plumes inject their warm water may be very different on present day Enceladus and Europa than that assumed in our study. For example, one could consider a scenario in which Enceladus' ocean temperature is initially homogeneous and warm, heavy water, injected from the hydrothermal vents spreads along the bottom as suggested by our calculations. This process would lead to a gradual build up of a warm dense layer along the bottom with a light layer above it (assuming no flow into the porous rocky core). Over a long period of geological time, accumulation of warm water at the bottom would build up so much heat in the bottom layer that the thermal expansion coefficient would ultimately become positive. This would drive convection in a thick ocean layer overlain by a linearly stratified colder water layer under the ice shell (Kang et al., 2022; Zeng & Jansen, 2021). In this case, we speculate that the full plume dynamics may behave differently compared to the end-members studied in our analysis. Whether the convection would be continuous or intermittent should be a topic of further study, taking into account effects of the large scale ocean circulation.

7 Conclusions

For terrestrial seawater with salinity exceeding $22\,\mathrm{g\,kg^{-1}}$, water heated by the hydrothermal vents becomes buoyant and rises. However, as argued recently by Kang et al. (2022), Enceladus may have an ocean which is fresher than that on earth, in line with the chemical equilibrium state obtained from consideration of the Enceladus' water-rock ratio in laboratory experiments (Zolotov, 2007; Zolotov & Postberg, 2014; Glein et al., 2018a). As shown in fig. 1a,c, and e, the value of α can be negative for a wide range of depths if the temperature is between -2 to 2°C. In such a case, gravity currents spreading along the sea floor is a more likely scenario on Enceladus than plumes reaching all the way to the surface.

In contrast, in the case of Europa, the ocean is expected to be more saline or have dissolved components which increase the thermal expansion coefficient of seawater. Additionally, its gravity is stronger and so buoyancy fluxes large, suggesting that plumes might reach all the way to the ice shell. Even if Europa turns out to be fresh, the depth of Europa's ocean and its higher gravity means that pressure effects would be a more prominent factor in setting the thermodynamic equation of state rather than temperature and salinity. Fig. 1a shows that negative values of α can only be achieved at extremely low salinities ($< 5\,\mathrm{psu}$) and shallow depths ($\sim 5\,\mathrm{km}$). Thus, even if Europa's ocean is fresh, we expect that plumes of buoyant fluid could indeed rise to the surface as postulated in Goodman et al. (2004); Goodman and Lenferink (2012).

Overall, this study uncovers a fundamental distinction in hydrothermal plume behavior based on the salinity of ambient water. This distinction becomes especially important for Enceladus but may not be substantial for Europa. Further, these results could potentially influence the decision-making process on choosing an icy moon to visit, at least in the short term. On a moon like Europa, which is likely to have more vigorous convection and more efficient seafloor to ice-shell transport which leaves its imprint on the ice shell. Thus, if the primary icy-ocean world habitable interface is the seafloor, it may be a more appealing prospect to focus on Europa than Enceladus because our current technological limitations make ice shells much more accessible than deep ocean. On the other hand, Enceladus's deep ocean could be stratified potentially providing chemical gradients for chemosynthetic life to thrive even within the ocean instead of just the seafloor.

Acknowledgments

This work was carried out in the Department of Earth, Atmospheric and Planetary Science (EAPS) in MIT. TM, WK acknowledges endowed funds in EAPS. JM and SB ac-

knowledges part-support from NASA Astrobiology Grant 80NSSC19K1427 "Exploring Ocean Worlds". We all thank "Exploring Ocean Worlds" for helpful support and discussions.

Oceananigans.jl (Ramadhan et al., 2020) was used to perform numerical simulations used in this study. Data from the numerical simulations and analysis code used in this study is available at Bire (2023).

References

Ashkenazy, Y., & Tziperman, E. (2021, Nov). Dynamic Europa ocean shows transient Taylor columns and convection driven by ice melting and salinity. *Nat. Commun.*, *12*(1). Retrieved from http://dx.doi.org/10.1038/s41467-021-26710-0 doi: 10.1038/s41467-021-26710-0

Beuthe, M., Rivoldini, A., & Trinh, A. (2016, Oct). Enceladus's and Dione's floating ice shells supported by minimum stress isostasy. *Geophys. Res. Lett.*, *43*(19), 10,088-10,096. Retrieved from http://dx.doi.org/10.1002/2016GL070650 doi: 10.1002/2016gl070650

Bire, S. (2023). *Juicymoons plumes.* Zenodo. Retrieved from https://zenodo.org/record/7502389 doi: 10.5281/ZENODO.7502389

Bire, S., Kang, W., Ramadhan, A., Campin, J., & Marshall, J. (2022, Mar). Exploring ocean circulation on icy moons heated from below. *J. Geophys. Res. Planets*, *127*(3). Retrieved from http://dx.doi.org/10.1029/2021JE007025 doi: 10.1029/2021je007025

Běhounková, M., Tobie, G., Choblet, G., Kervazo, M., Melwani Daswani, M., Dumoulin, C., & Vance, S. D. (2021, Feb). Tidally induced magmatic pulses on the oceanic floor of Jupiter's moon Europa. *Geophys. Res. Lett.*, *48*(3). Retrieved from http://dx.doi.org/10.1029/2020GL090077 doi: 10.1029/2020gl090077

Cable, M. L., Porco, C., Glein, C. R., German, C. R., MacKenzie, S. M., Neveu, M., ... Núñez, J. (2021, Jul). The science case for a return to Enceladus. *Planet. Sci. J.*, *2*(4), 132. Retrieved from http://dx.doi.org/10.3847/PSJ/abfb7a doi: 10.3847/psj/abfb7a

Čadek, O., Souček, O., & Běhounková, M. (2019, Dec). Is Airy isostasy applicable to icy moons? *Geophys. Res. Lett.*, *46*(24), 14299–14306. Retrieved from http://dx.doi.org/10.1029/2019GL085903 doi: 10.1029/2019gl085903

Čadek, O., Tobie, G., Van Hoolst, T., Massé, M., Choblet, G., Lefèvre, A., ... Trinh, A. (2016, Jun). Enceladus's internal ocean and ice shell constrained from cassini gravity, shape, and libration data. *Geophys. Res. Lett.*, *43*(11), 5653–5660. Retrieved from http://dx.doi.org/10.1002/2016GL068634 doi: 10.1002/2016gl068634

Cario, A., Oliver, G. C., & Rogers, K. L. (2019, Sep). Exploring the deep marine biosphere: Challenges, innovations, and opportunities. *Front. Earth Sci.*, *7*. Retrieved from http://dx.doi.org/10.3389/feart.2019.00225 doi: 10.3389/feart.2019.00225

Choblet, G., Tobie, G., Buch, A., Čadek, O., Barge, L. M., Bēhounková, M., ... Van Hoolst, T. (2021, Nov). Enceladus as a potential oasis for life: Science goals and investigations for future explorations. *Exp. Astron.*. Retrieved from http://dx.doi.org/10.1007/s10686-021-09808-7 doi: 10.1007/s10686-021-09808-7

Choblet, G., Tobie, G., Sotin, C., Běhounková, M., Čadek, O., Postberg, F., & Souček, O. (2017, Nov). Powering prolonged hydrothermal activity inside Enceladus. *Nat. Astron.*, *1*(12), 841–847. Retrieved from http://dx.doi.org/10.1038/s41550-017-0289-8 doi: 10.1038/s41550-017-0289-8

Dai, A., & Wu, C.-S. (2016, Sep). High-resolution simulations of cylindrical grav-

ity currents in a rotating system. *J. Fluid Mech.*, *806*, 71–101. Retrieved from http://dx.doi.org/10.1017/jfm.2016.598 doi: 10.1017/jfm.2016.598

Dai, A., & Wu, C.-S. (2018, Feb). High-resolution simulations of unstable cylindrical gravity currents undergoing wandering and splitting motions in a rotating system. *Phys. Fluids*, *30*(2), 026601. Retrieved from http://dx.doi.org/10.1063/1.5011070 doi: 10.1063/1.5011070

Ede, A. J. (1956, Nov). The influence of anomalous expansion on natural convection in water. *Appl. Sci. Res.*, *5*(6), 458–460. Retrieved from http://dx.doi.org/10.1007/BF03184607 doi: 10.1007/bf03184607

Fifer, L. M., Catling, D. C., & Toner, J. D. (2022, Aug). Chemical fractionation modeling of plumes indicates a gas-rich, moderately alkaline Enceladus ocean. *Planet. Sci. J.*, *3*(8), 191. Retrieved from http://dx.doi.org/10.3847/PSJ/ac7a9f doi: 10.3847/psj/ac7a9f

Fox-Powell, M. G., & Cousins, C. R. (2021). Partitioning of crystalline and amorphous phases during freezing of simulated enceladus ocean fluids. *Journal of Geophysical Research: Planets*, *126*(1), e2020JE006628.

Glass, J., Dierssen, H., Glein, C., Schmidt, B., & Winebrenner, D. (2022). Defining and characterizing habitable environments in ocean world systems. *Oceanography*. Retrieved from http://dx.doi.org/10.5670/oceanog.2021.414 doi: 10.5670/oceanog.2021.414

Glein, C., Postberg, F., & Vance, S. (2018a). The geochemistry of enceladus: Composition and controls. *Enceladus and the icy moons of Saturn*, *39*.

Glein, C., Postberg, F., & Vance, S. D. (2018b, Jan). The geochemistry of Enceladus: Composition and controls. In (chap. 3). The University of Arizona Press. Retrieved from http://dx.doi.org/10.2458/azu_uapress_9780816537075-ch003 doi: 10.2458/azu_uapress_9780816537075-ch003

Goodman, J. C., Collins, G. C., Marshall, J., & Pierrehumbert, R. T. (2004). Hydrothermal plume dynamics on Europa: Implications for chaos formation. *J. Geophys. Res.*, *109*(E3). Retrieved from http://dx.doi.org/10.1029/2003JE002073 doi: 10.1029/2003je002073

Goodman, J. C., & Lenferink, E. (2012, Nov). Numerical simulations of marine hydrothermal plumes for Europa and other icy worlds. *Icarus*, *221*(2), 970–983. Retrieved from http://dx.doi.org/10.1016/j.icarus.2012.08.027 doi: 10.1016/j.icarus.2012.08.027

Griffiths, R. W., & Linden, P. F. (1981, Apr). The stability of vortices in a rotating, stratified fluid. *J. Fluid Mech.*, *105*(-1), 283. Retrieved from http://dx.doi.org/10.1017/S0022112081003212 doi: 10.1017/s0022112081003212

Hand, K., & Chyba, C. (2007, August). Empirical constraints on the salinity of the europan ocean and implications for a thin ice shell. *Icarus*, *189*(2), 424–438.

Hand, K., Sotin, C., Hayes, A., & Coustenis, A. (2020, Jul). On the habitability and future exploration of ocean worlds. *Space Sci. Rev.*, *216*(5). Retrieved from http://dx.doi.org/10.1007/s11214-020-00713-7 doi: 10.1007/s11214-020-00713-7

Hansen, C. J., Esposito, L., Stewart, A. I. F., Colwell, J., Hendrix, A., Pryor, W., ... West, R. (2006, Mar). Enceladus' water vapor plume. *Science*, *311*(5766), 1422–1425. Retrieved from http://dx.doi.org/10.1126/science.1121254 doi: 10.1126/science.1121254

Helfrich, K. R. (1994, Jan). Thermals with background rotation and stratification. *J. Fluid Mech.*, *259*, 265–280. Retrieved from http://dx.doi.org/10.1017/S0022112094000121 doi: 10.1017/s0022112094000121

Hemingway, D. J., & Mittal, T. (2019, Nov). Enceladus's ice shell structure as a window on internal heat production. *Icarus*, *332*, 111–131. Retrieved from http://dx.doi.org/10.1016/j.icarus.2019.03.011 doi: 10.1016/j.icarus.2019.03.011

Hsu, H.-W., Postberg, F., Sekine, Y., Shibuya, T., Kempf, S., Horányi, M., ...

Srama, R. (2015, Mar). Ongoing hydrothermal activities within Enceladus. *Nature*, *519*(7542), 207–210. Retrieved from http://dx.doi.org/10.1038/nature14262 doi: 10.1038/nature14262

Ingersoll, A. P., & Nakajima, M. (2016). Controlled boiling on enceladus. 2. model of the liquid-filled cracks. *Icarus*, *272*, 319–326.

Ivanov, D., & Nikolov, S. (2020, Jul). The anomalous thermal expansion of water. *Phys. Educ.*, *55*(5), 055008. Retrieved from http://dx.doi.org/10.1088/1361-6552/ab9480 doi: 10.1088/1361-6552/ab9480

Jones, H., & Marshall, J. (1993, Jun). Convection with rotation in a neutral ocean: A study of open-ocean deep convection. *J. Phys. Oceanogr.*, *23*(6), 1009–1039. Retrieved from http://dx.doi.org/10.1175/1520-0485(1993)023<1009:CWRIAN>2.0.CO;2 doi: 10.1175/1520-0485(1993)023⟨1009:cwrian⟩2.0.co;2

Kang, W., Mittal, T., Bire, S., Campin, J.-M., & Marshall, J. (2022, Jul). How does salinity shape ocean circulation and ice geometry on Enceladus and other icy satellites? *Sci. Adv.*, *8*(29). Retrieved from http://dx.doi.org/10.1126/sciadv.abm4665 doi: 10.1126/sciadv.abm4665

Khawaja, N., Postberg, F., Hillier, J., Klenner, F., Kempf, S., Nölle, L., ... Srama, R. (2019, Oct). Low-mass nitrogen-, oxygen-bearing, and aromatic compounds in Enceladean ice grains. *Monthly Notices of the Royal Astronomical Society*, *489*(4), 5231–5243. Retrieved from http://dx.doi.org/10.1093/mnras/stz2280 doi: 10.1093/mnras/stz2280

Kvorka, J., Čadek, O., Tobie, G., & Choblet, G. (2018, Aug). Does Titan's long-wavelength topography contain information about subsurface ocean dynamics? *Icarus*, *310*, 149–164. Retrieved from http://dx.doi.org/10.1016/j.icarus.2017.12.010 doi: 10.1016/j.icarus.2017.12.010

MacKenzie, S. M., Neveu, M., Davila, A. F., Lunine, J. I., Cable, M. L., Phillips-Lander, C. M., ... Heldmann, J. (2022, Jun). Science objectives for flagship-class mission concepts for the search for evidence of life at Enceladus. *Astrobiology*, *22*(6), 685–712. Retrieved from http://dx.doi.org/10.1089/ast.2020.2425 doi: 10.1089/ast.2020.2425

Maxworthy, T., & Narimousa, S. (1994, May). Unsteady, turbulent convection into a homogeneous, rotating fluid,with oceanographic applications. *J. Phys. Oceanogr.*, *24*(5), 865–887. Retrieved from http://dx.doi.org/10.1175/1520-0485(1994)024<0865:UTCIAH>2.0.CO;2 doi: 10.1175/1520-0485(1994)024⟨0865:utciah⟩2.0.co;2

Millero, F. J., Feistel, R., Wright, D. G., & McDougall, T. J. (2008, Jan). The composition of standard seawater and the definition of the reference-composition salinity scale. *Deep Sea Res. Part I Oceanogr. Res. Pap.*, *55*(1), 50–72. Retrieved from http://dx.doi.org/10.1016/j.dsr.2007.10.001 doi: 10.1016/j.dsr.2007.10.001

Nimmo, F., & Pappalardo, R. T. (2016, Aug). Ocean worlds in the outer solar system. *J. Geophys. Res. Planets*, *121*(8), 1378–1399. Retrieved from http://dx.doi.org/10.1002/2016JE005081 doi: 10.1002/2016je005081

Porco, C. C., Helfenstein, P., Thomas, P. C., Ingersoll, A. P., Wisdom, J., West, R., ... Squyres, S. (2006, Mar). Cassini observes the active south pole of Enceladus. *Science*, *311*(5766), 1393–1401. Retrieved from http://dx.doi.org/10.1126/science.1123013 doi: 10.1126/science.1123013

Postberg, F., Kempf, S., Schmidt, J., Brilliantov, N., Beinsen, A., Abel, B., ... Srama, R. (2009). Sodium salts in e-ring ice grains from an ocean below the surface of enceladus. *Nature*, *459*(7250), 1098–1101.

Postberg, F., Khawaja, N., Abel, B., Choblet, G., Glein, C. R., Gudipati, M. S., ... Waite, J. H. (2018, Jun). Macromolecular organic compounds from the depths of Enceladus. *Nature*, *558*(7711), 564–568. Retrieved from http://dx.doi.org/10.1038/s41586-018-0246-4 doi: 10.1038/s41586-018-0246-4

Postberg, F., Klenner, F., Zou, Z., Hillier, J. K., Khawaja, N., Nölle, L., & Schmidt,

J. (2022, Sep). Detection of phosphates originating from Enceladus' ocean by Cassini's cosmic dust analyzer. *Europlanet Science Congress 2022, Granada, Spain, 18–23 Sep 2022, EPSC2022-639*. Retrieved from http://dx.doi.org/10.5194/epsc2022-639 doi: 10.5194/epsc2022-639

Ramadhan, A., Wagner, G., Hill, C., Campin, J.-M., Churavy, V., Besard, T., ... Marshall, J. (2020, Sep). Oceananigans.jl: Fast and friendly geophysical fluid dynamics on GPUs. *J. Open Source Softw.*, *5*(53), 2018. Retrieved from http://dx.doi.org/10.21105/joss.02018 doi: 10.21105/joss.02018

Roquet, F., Madec, G., Brodeau, L., & Nycander, J. (2015, Oct). Defining a simplified yet "realistic" equation of state for seawater. *J. Phys. Oceanogr.*, *45*(10), 2564–2579. Retrieved from http://dx.doi.org/10.1175/JPO-D-15-0080.1 doi: 10.1175/jpo-d-15-0080.1

Rovira-Navarro, M., Katz, R. F., Liao, Y., van der Wal, W., & Nimmo, F. (2022, May). The tides of Enceladus' porous core. *J. Geophys. Res. Planets*, *127*(5). Retrieved from http://dx.doi.org/10.1029/2021JE007117 doi: 10.1029/2021je007117

Saunders, P. M. (1973, Jan). The instability of a baroclinic vortex. *J. Phys. Oceanogr.*, *3*(1), 61–65. Retrieved from http://dx.doi.org/10.1175/1520-0485(1973)003<0061:TIOABV>2.0.CO;2 doi: 10.1175/1520-0485(1973)003⟨0061:tioabv⟩2.0.co;2

Sekine, Y., Shibuya, T., Postberg, F., Hsu, H.-W., Suzuki, K., Masaki, Y., ... Sirono, S.-i. (2015, Oct). High-temperature water–rock interactions and hydrothermal environments in the chondrite-like core of Enceladus. *Nat. Commun.*, *6*(1). Retrieved from http://dx.doi.org/10.1038/ncomms9604 doi: 10.1038/ncomms9604

Soderlund, K. M. (2019, Aug). Ocean dynamics of outer solar system satellites. *Geophys. Res. Lett.*, *46*(15), 8700–8710. Retrieved from http://dx.doi.org/10.1029/2018GL081880 doi: 10.1029/2018gl081880

Soderlund, K. M., Schmidt, B. E., Wicht, J., & Blankenship, D. D. (2013, Dec). Ocean-driven heating of Europa's icy shell at low latitudes. *Nat. Geosci.*, *7*(1), 16–19. Retrieved from http://dx.doi.org/10.1038/NGEO2021 doi: 10.1038/ngeo2021

Speer, K. G., & Marshall, J. (1995, Nov). The growth of convective plumes at seafloor hot springs. *J. Mar. Res.*, *53*(6), 1025–1057. Retrieved from http://dx.doi.org/10.1357/0022240953212972 doi: 10.1357/0022240953212972

Steel, E. L., Davila, A., & McKay, C. P. (2017, Sep). Abiotic and biotic formation of amino acids in the Enceladus ocean. *Astrobiology*, *17*(9), 862–875. Retrieved from http://dx.doi.org/10.1089/ast.2017.1673 doi: 10.1089/ast.2017.1673

Tebo, B. M., Nealson, K. H., Emerson, S., & Jacobs, L. (1984, Nov). Microbial mediation of Mn(II) and Co(II) precipitation at the O_2/H_2S interfaces in two anoxic fjords. *Limnol. Oceanogr.*, *29*(6), 1247–1258. Retrieved from http://dx.doi.org/10.4319/lo.1984.29.6.1247 doi: 10.4319/lo.1984.29.6.1247

Thomas, P., Tajeddine, R., Tiscareno, M., Burns, J., Joseph, J., Loredo, T., ... Porco, C. (2016, Jan). Enceladus's measured physical libration requires a global subsurface ocean. *Icarus*, *264*, 37–47. Retrieved from http://dx.doi.org/10.1016/j.icarus.2015.08.037 doi: 10.1016/j.icarus.2015.08.037

Trumbo, S. K., Brown, M. E., & Hand, K. P. (2019, Jun). Sodium chloride on the surface of Europa. *Sci. Adv.*, *5*(6), eaaw7123. Retrieved from http://dx.doi.org/10.1126/sciadv.aaw7123 doi: 10.1126/sciadv.aaw7123

Vance, S., Bouffard, M., Choukroun, M., & Sotin, C. (2014, Jun). Ganymedes internal structure including thermodynamics of magnesium sulfate oceans in contact with ice. *Planetary and Space Science*, *96*, 62–70. Retrieved from http://

673 dx.doi.org/10.1016/j.pss.2014.03.011 doi: 10.1016/j.pss.2014.03.011
674 Vance, S., Panning, M. P., Stähler, S., Cammarano, F., Bills, B. G., Tobie,
675 G., ... Banerdt, B. (2018, Jan). Geophysical investigations of habit-
676 ability in ice-covered ocean worlds. *J. Geophys. Res. Planets*, *123*(1),
677 180–205. Retrieved from http://dx.doi.org/10.1002/2017JE005341 doi:
678 10.1002/2017je005341
679 Van Hoolst, T., Baland, R.-M., & Trinh, A. (2016, Oct). The diurnal libration and
680 interior structure of Enceladus. *Icarus*, *277*, 311–318. Retrieved from http://
681 dx.doi.org/10.1016/j.icarus.2016.05.025 doi: 10.1016/j.icarus.2016.05
682 .025
683 Waite, J. H., Glein, C. R., Perryman, R. S., Teolis, B. D., Magee, B. A., Miller,
684 G., ... Bolton, S. J. (2017, Apr). Cassini finds molecular hydrogen in the
685 Enceladus plume: Evidence for hydrothermal processes. *Science*, *356*(6334),
686 155–159. Retrieved from http://dx.doi.org/10.1126/science.aai8703
687 doi: 10.1126/science.aai8703
688 Zeng, Y., & Jansen, M. F. (2021). Ocean circulation on enceladus with a high-versus
689 low-salinity ocean. *The Planetary Science Journal*, *2*(4), 151.
690 Zolotov, M. Y. (2007). An oceanic composition on early and today's enceladus. *Geo-*
691 *physical Research Letters*, *34*(23).
692 Zolotov, M. Y., & Postberg, F. (2014). Can nano-phase silica originate from chon-
693 dritic fluids? the application to enceladus' sio2 particles. *LPI*(1777), 2496.

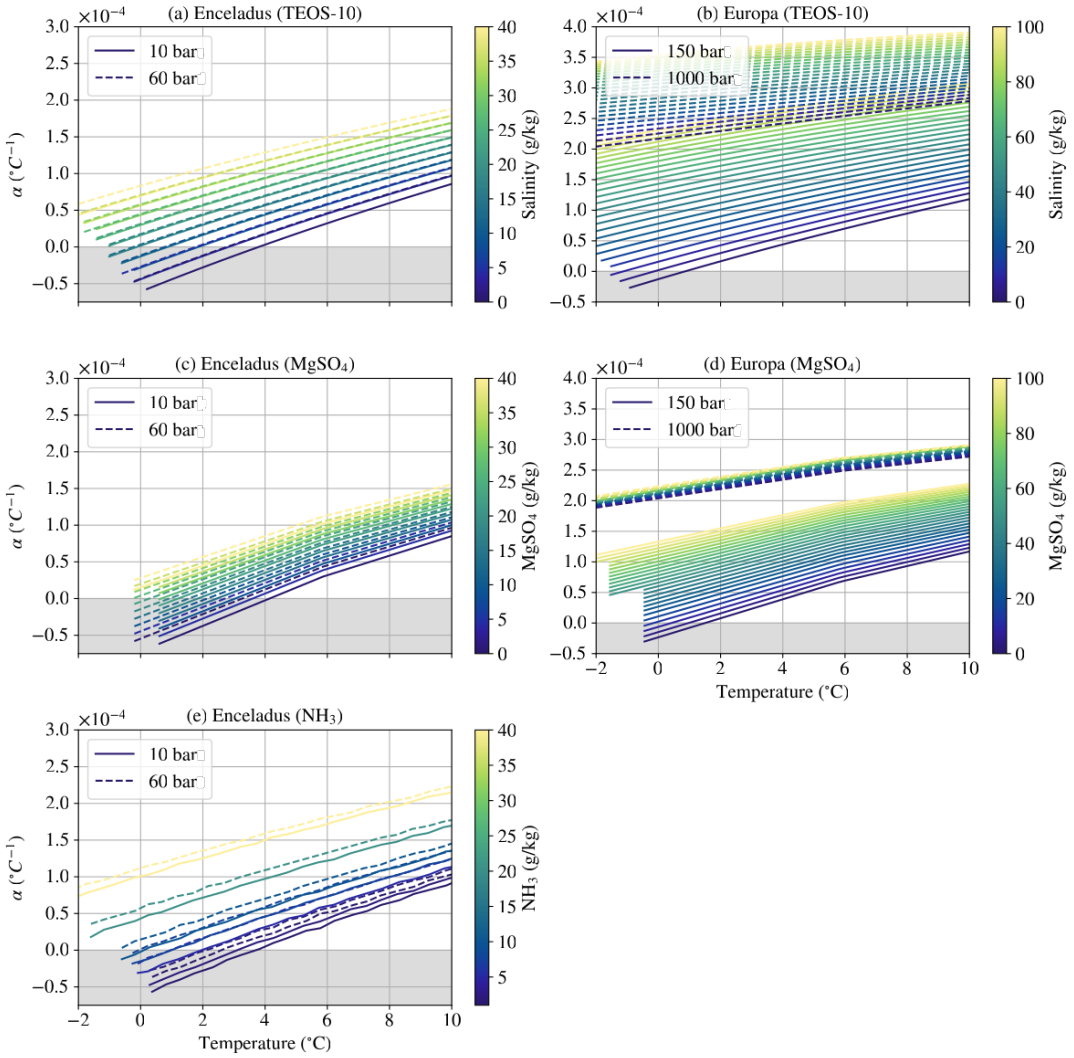

Figure 1. The thermal expansion coefficient of (a) seawater, (c) water rich in magnesium sulphate, and (e) water rich in ammonia is shown as a function of temperature (x-axis) and salt concentration (shading). The relationships are plotted for pressures of 10,30, and 60 bar by solid, dashed, and dotted lines, respectively, roughly corresponding to depths of 5, 25, and 50 km on Enceladus. Thermal expansion coefficient of (b) seawater and (d) water rich in magnesium sulphate are shown at pressures of 150, 600, 1000, and 2000 bar, roughly corresponding to depths of 5, 50, 100, and 150 km on Europa. The region shaded in grey picks out parameter values in which the thermal expansion coefficient becomes negative.

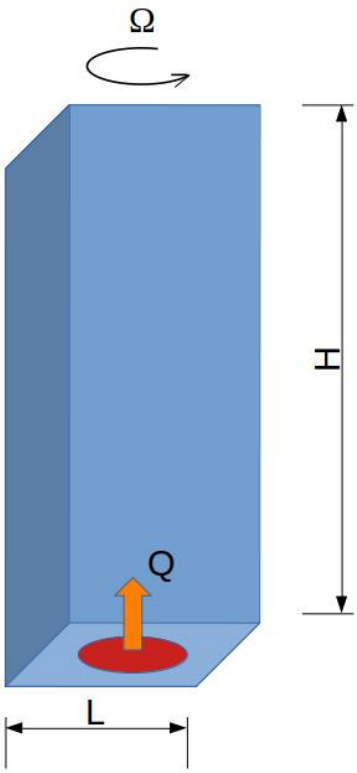

Figure 2. The configuration of the numerical model. The domain size is $10 \times 10 \times 40\,\mathrm{km}^3$. A heating patch is applied at the bottom with an area of $1 \times 1\,\mathrm{km}^2$ shown in red which acts as the source of the hydrothermal plume. The resolution of the model is 40 m in the horizontal and 80 m in the vertical.

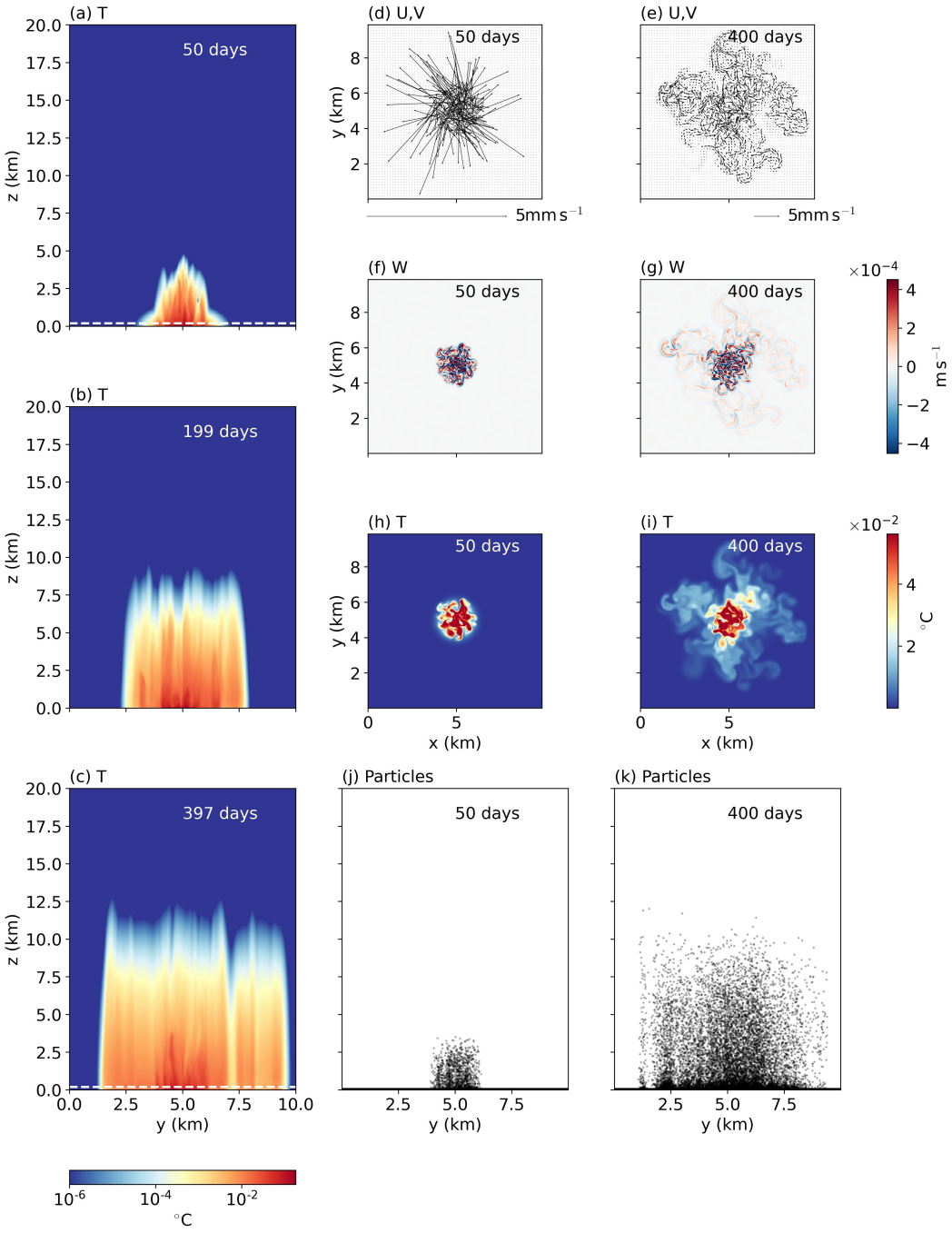

Figure 3. Panels a, b, and c show the meridional sections of temperature at $x = 5$ km due to a hydrothermal plume for a saline ocean at 50, 200, and 400 rotation periods, respectively. Panels d and e show the velocity vectors 80 m above the bottom at 50 and 400 rotation periods, respectively. Panels f and g show the vertical velocity at 50 and 400 rotation periods, respectively. Panels h and i show the plan view of temperature 80 m above the bottom at 50 and 400 rotation periods, respectively. Panels j and k show the meridional sections at $x = 5$ km of particles initially released at the bottom.

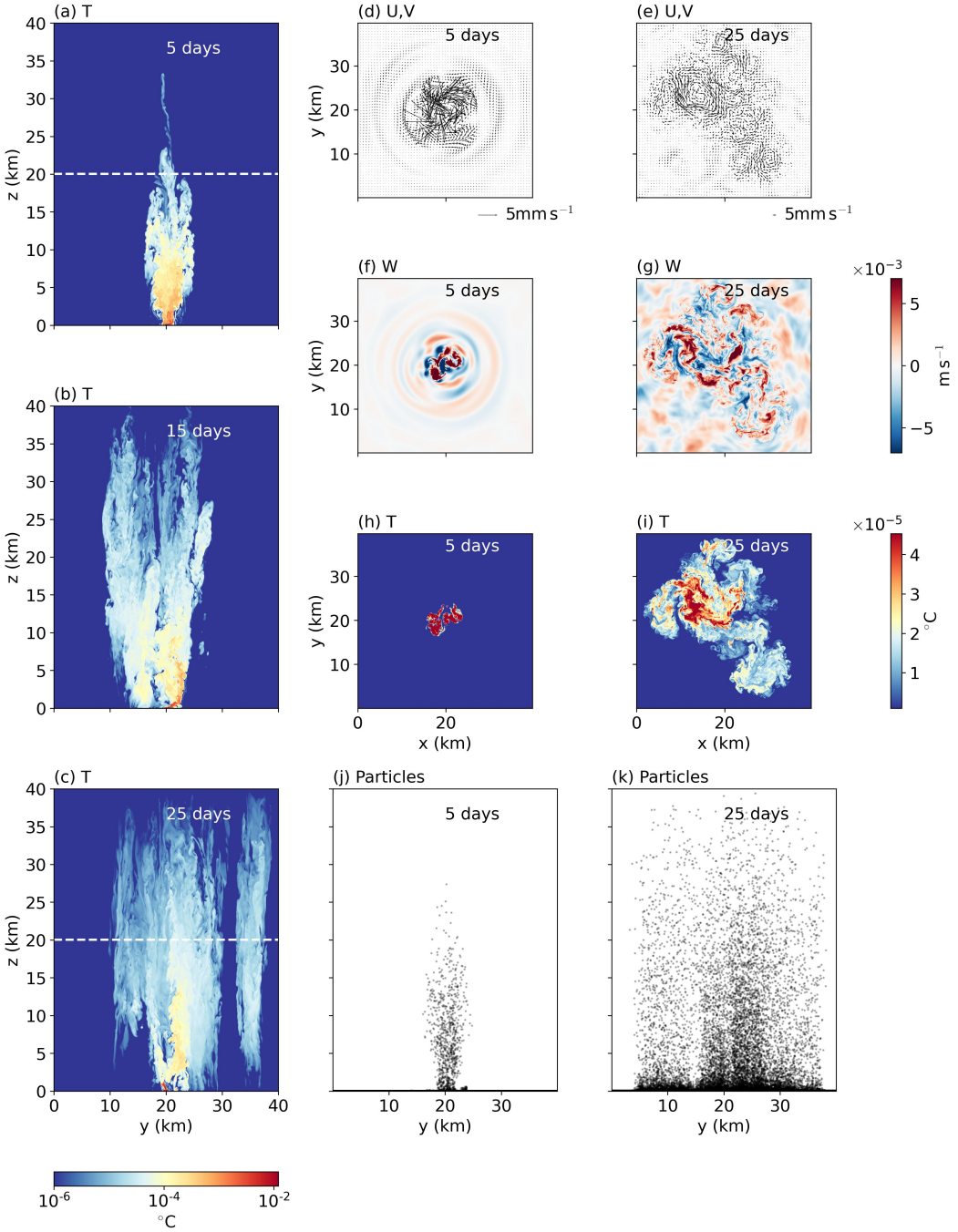

Figure 4. Panels a, b, and c show the meridional sections of temperature at $x = 20$ km due to a hydrothermal plume for a saline ocean at 5, 15, and 25 rotation periods, respectively. Panels d and e show the velocity vectors 20 km above the bottom at 5 and 25 rotation periods, respectively. Panels f and g show the vertical velocity at 5 and 25 rotation periods, respectively. Panels h and i show the plan view of temperature 20 km above the bottom at 5 and 25 rotation periods, respectively. Panels j and k show the meridional sections at $x = 20$ km of particles initially released at the bottom.

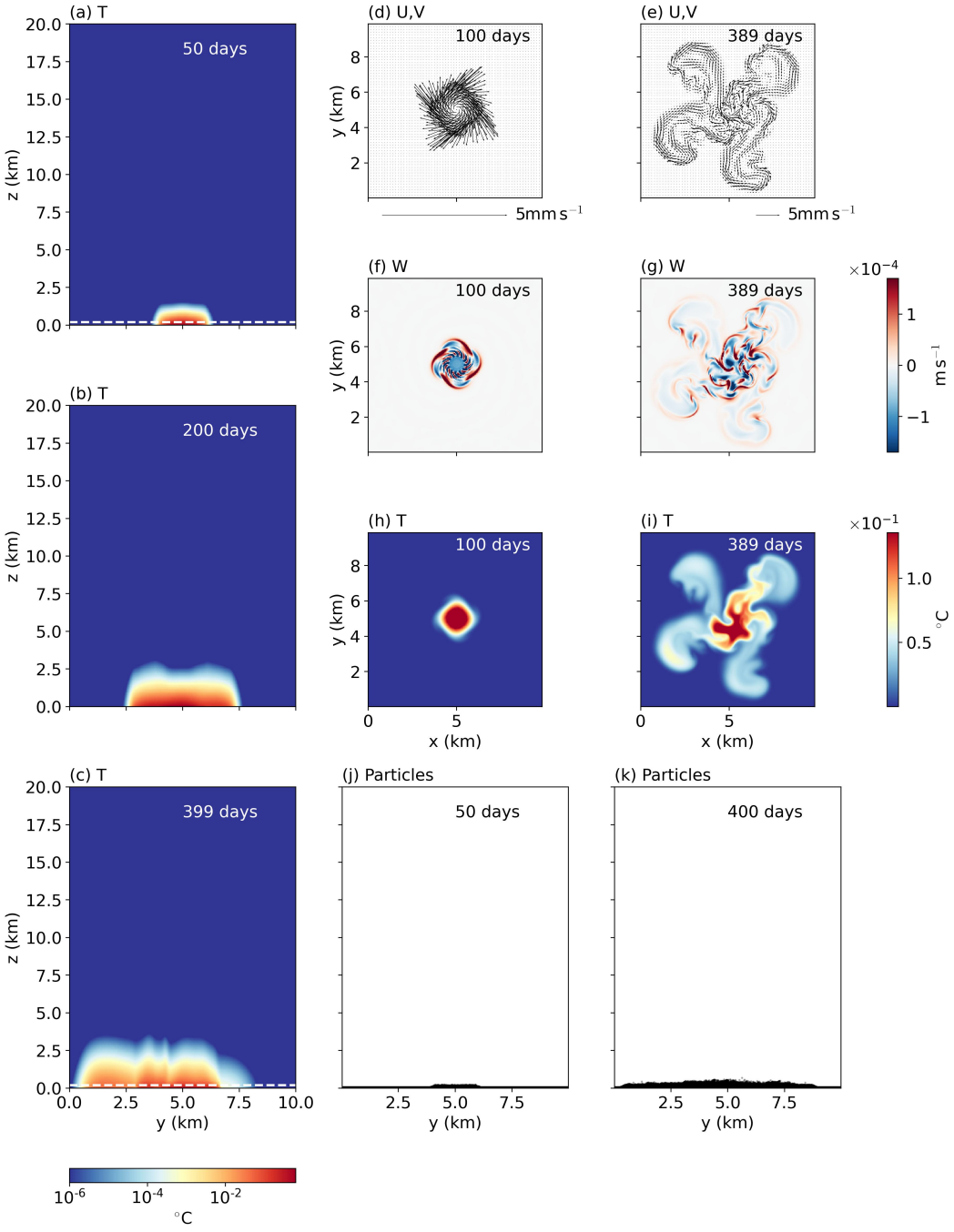

Figure 5. Panels a, b, and c show the meridional sections of temperature at $x = 5$ km due to a hydrothermal plume for a fresh ocean at 50, 200, and 400 rotation periods, respectively. Panels d and e show the velocity vectors 80 m above the bottom at 50 and 400 rotation periods, respectively. Panels f and g show the vertical velocity at 50 and 400 rotation periods, respectively. Panels h and i show the plan view of temperature 80 m above the bottom at 50 and 400 rotation periods, respectively. Panels j and k show the meridional sections at $x = 5$ km of particles initially released at the bottom.

Figure 1.

(a) Enceladus (TEOS-10)

(b) Europa (TEOS-10)

(c) Enceladus ($MgSO_4$)

(d) Europa ($MgSO_4$)

(e) Enceladus (NH_3)

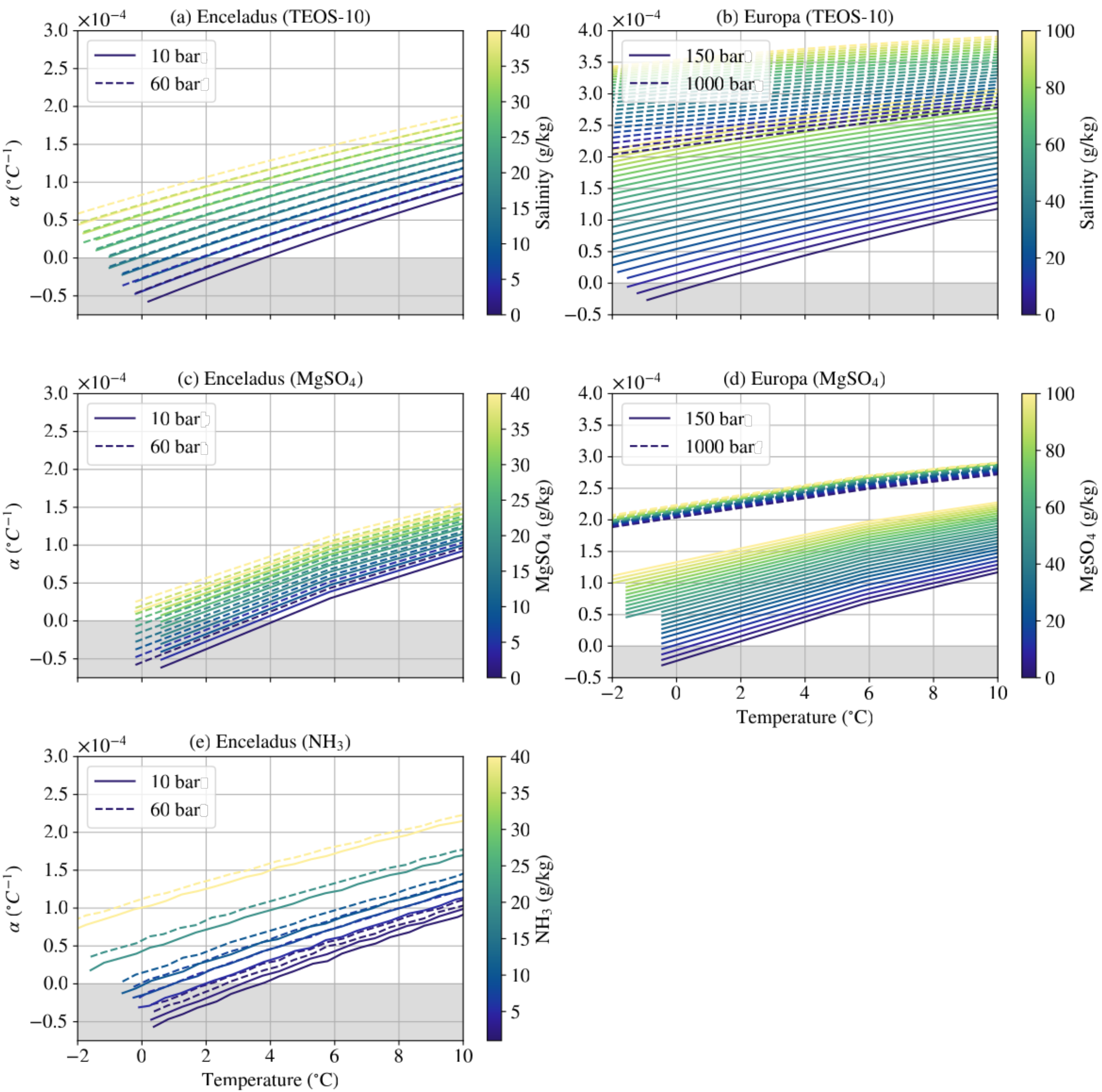

Figure 2.

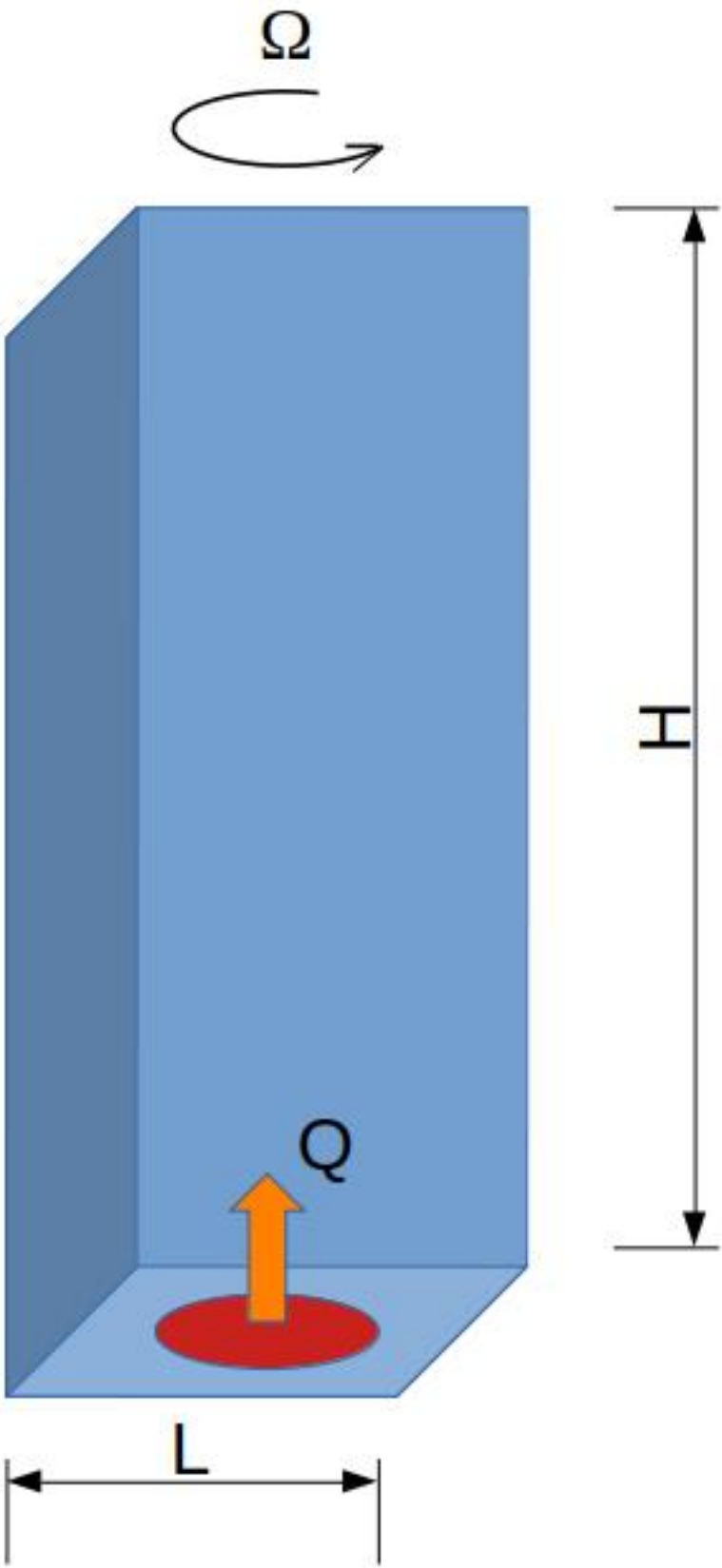
Ω
H
Q
L

Figure 3.

(a) T
50 days
(b) T
199 days
(c) T
397 days
z (km)
y (km)
10^{-6} 10^{-4} 10^{-2}
°C
(d) U,V
50 days
(e) U,V
400 days
5mm s^{-1}
(f) W
50 days
(g) W
400 days
$\times 10^{-4}$
m s^{-1}
(h) T
50 days
(i) T
400 days
$\times 10^{-2}$
°C
x (km)
(j) Particles
50 days
(k) Particles
400 days

Figure 4.

(a) T
5 days
z (km)
(b) T
15 days
z (km)
(c) T
25 days
z (km)
y (km)
10^{-6} 10^{-4} 10^{-2}
°C
(d) U,V
5 days
y (km)
5mm s^{-1}
(e) U,V
25 days
5mm s^{-1}
(f) W
5 days
y (km)
(g) W
25 days
$\times 10^{-3}$
5
0
−5
m s^{-1}
(h) T
5 days
y (km)
x (km)
(i) T
25 days
x (km)
$\times 10^{-5}$
4
3
2
1
°C
(j) Particles
5 days
y (km)
(k) Particles
25 days
y (km)

Figure 5.

(a) T
50 days
(b) T
200 days
(c) T
399 days
z (km)
y (km)
10^{-6} 10^{-4} 10^{-2}
°C
(d) U,V
100 days
(e) U,V
389 days
5mm s^{-1}
(f) W
100 days
(g) W
389 days
$\times 10^{-4}$
m s^{-1}
(h) T
100 days
(i) T
389 days
$\times 10^{-1}$
°C
x (km)
(j) Particles
50 days
(k) Particles
400 days